01 Jan 2022

Self-Vernier Effect-Assisted Optical Fiber Sensor based on Microwave Photonics and its Machine Learning Analysis

Chen Zhu
Missouri University of Science and Technology, cznwq@mst.edu

Jie Huang
Missouri University of Science and Technology, jieh@mst.edu

Recommended Citation

C. Zhu and J. Huang, "Self-Vernier Effect-Assisted Optical Fiber Sensor based on Microwave Photonics and its Machine Learning Analysis," *Journal of Lightwave Technology*, Institute of Electrical and Electronics Engineers; Optica, Jan 2022.
The definitive version is available at https://doi.org/10.1109/JLT.2022.3227247

Self-Vernier Effect-Assisted Optical Fiber Sensor Based on Microwave Photonics and Its Machine Learning Analysis

Chen Zhu, *Member, IEEE*, and Jie Huang, *Senior Member, IEEE*

***Abstract*—Optical Vernier effect has been recently demonstrated as a tool to enhance the sensitivity of optical fiber interferometric sensors and has become a hot topic in the last few years. The generation of the Vernier effect relies on the superposition of interferograms of two interferometers (a sensing one and a reference one) with marginally different optical path differences (OPDs), where an amplitude modulation-like signal is sustained in the output spectrum. The Vernier modulation envelope exhibits significantly magnified sensitivity in response to external perturbations, compared to the individual sensing interferometer, providing a new route to new generations of ultra-sensitive optical fiber sensors. However, the construction of a Vernier effect-based sensor needs careful integration of two interferometers with a precise OPD deviation, which is challenging if not impossible sometimes. Additionally, the interrogation of a Vernier effect-based sensor requires the acquisition of its spectrum in a broad wavelength (frequency) window with a large number of sampling points, followed by cumbersome processing for the extraction of the Vernier envelope signal. In this article, we propose a new concept of the self-Vernier effect for the sensitivity improvement of optical fiber sensors. A proof-of-concept demonstration is performed using a single low-coherent microwave-photonic Fabry-Perot interferometer (FPI) with an addition of an auxiliary delay path. The self-Vernier effect is obtained by the overlap between the microwave interferogram of the FPI and its slightly time-delayed one. Detailed analyses regarding the principle, mathematical modeling, and experimental investigation are given. Moreover, we propose and demonstrate a new demodulation approach to the Vernier effect-based sensor through machine learning analysis by directly and statistically learning the embedded relation between the measurand of interest and the output spectrum. It is appreciated that the necessity of the frequency observation window and the number of sampling points can be remarkably reduced through machine learning analysis. The present interrogation strategy is highly generalizable and can be readily applied to optical-domain Vernier effect-based optical fiber sensors.**

***Index Terms*—Interferometric sensors, machine learning, microwave photonics, vernier effect.**

Manuscript received 9 August 2022; revised 31 October 2022; accepted 3 December 2022. Date of publication 7 December 2022; date of current version 16 March 2023. This work of Chen Zhu was supported by the Research Initiation Project of Zhejiang Lab under Grant 2022ME0PI01. *(Corresponding author: Chen Zhu.)*

Chen Zhu is with the Research Center for Optical Fiber Sensing, Zhejiang Laboratory, Hangzhou 311100, China (e-mail: cz_chenzhu@163.com).

Jie Huang is with the Department of Electrical and Computer Engineering, Missouri University of Science and Technology, Rolla, MO 65409 USA (e-mail: jieh@mst.edu).

Color versions of one or more figures in this article are available at https://doi.org/10.1109/JLT.2022.3227247.

Digital Object Identifier 10.1109/JLT.2022.3227247

I. Introduction

THE optical Vernier effect has recently emerged as an effective approach to greatly enhancing the measurement sensitivity of optical fiber interferometric sensors since its first successful implementation on an optical fiber strain sensor based on two cascaded optical fiber ring resonators [1], [2], [3], [4], [5], [6]. To date, the optical Vernier effect has been demonstrated in various interferometers for the measurement of various physical and chemical parameters, such as temperature [7], [8], [9], strain [10], [11], [12], displacement [13], humidity [14], [15], refractive index [16], [17], [18], [19], etc. A comprehensive and critical overview of the recent development of Vernier effect-based optical fiber sensors can be found in [2], [3].

As an analog to the Vernier caliper where two scales are overlapped for the measurement, the generation of the optical Vernier effect relies on the overlap between the interference signals of two optical fiber interferometers with marginally different optical path differences (OPDs). One interferometer serves as the sensing device, while the other one is employed as the reference device. A typical amplitude modulation-like signal is sustained in the superimposed spectrum of a Vernier effect-based sensor, where the spectral shift of the Vernier modulation envelope is tracked as the reference variable in response to external perturbations. The shift of the Vernier envelope is significantly magnified, compared to the single sensing interferometer, and importantly, the magnification factor is inversely proportional to the OPD deviation of the two interferometers that constitute the Vernier sensor. Therefore, a smaller OPD deviation leads to a Vernier sensor with higher sensitivity. However, precisely controlling the OPD of an optical fiber interferometer is challenging and requires high-precision fabrication facilities such as a microscope system and femtosecond laser workstation [20], [21]. Besides, the integration of two interferometers in a single system is sometimes cumbersome. It is appreciated that very recently the Vernier effect has been demonstrated in a single interferometer with the assistance of either modal inference [22] or signal processing [23], paving the way to new generations of high-performance Vernier effect-based optical fiber sensors. In addition to the optical Vernier effect, the so-called microwave-photonic Vernier effect was also recently demonstrated, where two microwave-photonic interferometers (MWPIs) with slightly different OPDs were cascaded to produce the Vernier envelope that could be tracked for sensitivity-improved sensing [24], [25],

[26], [27]. The relatively large size of the MWPI has considerably relieved the stringent requirement of the fabrication accuracy of the OPD deviation to obtain a desired sensitivity magnification factor.

In this work, we propose a novel concept of the self-Vernier effect, which is used as a tool for the sensitivity magnification of MWPI. The self-Vernier effect is physically generated from a single interferometer and its time-delayed one, where the associated sensitivity magnification factor is controlled by adjusting the time delay. As a proof of concept, a single low-coherent microwave-photonic Fabry-Perot interferometer (FPI) with an addition of an auxiliary delay line is constructed for the measurement of axial strains. The self-Vernier effect is then obtained by the overlap between the microwave interferogram of the FPI and its slightly time-delayed one. The envelope signal generated by the self-Vernier effect is monitored in response to different axial strains applied to the FPI. The working principle, mathematical modeling, and experimental investigation for the self-Vernier effect-based FPI system are given in detail. The high flexibility and ease of adjustment of the self-Vernier effect are shown in comparison to the conventional two-interferometers-based Vernier effect.

An additional critical aspect that is investigated in this work is the demodulation of Vernier effect-based sensors. It is appreciated that a recent comprehensive review [3] pointed out that a huge downside of an optical Vernier effect-based sensor is the interrogator, which typically involves a broadband light source and an optical spectrum analyzer. The same challenge is occurring in the case of microwave-photonic Vernier effect-based sensors, including the proposed self-Vernier effect-based sensor. Meanwhile, in addition to the hardware, the signal demodulation for Vernier effect-based sensors, which requires multiple nonlinear approximations, is much more involved in comparison to conventional interferometric sensors. The two limiting aspects have significantly hindered the practical applications of Vernier effect-based sensors. The resounding success of machine learning applications in a diverse array of fields including photonics has motivated us to investigate the possibility of using machine learning as a tool for the demodulation of the proposed self-Vernier effect-based sensor, for the first time. We show that machine learning can directly learn the relationship between the measured raw spectrum (i.e., the superimposed spectrum consisting of dense interference fringes and envelopes) and the measurand of interest (e.g., tensile strain) and then predict unknown strains with high fidelity. What is also shown is that the stringent requirement of the measurement over a broad range of wavelengths (frequencies) is remarkably alleviated by employing machine learning-based analysis. Details regarding the capability of machine learning analysis for performance boosting (e.g., reduced sampling points and measurement bandwidth) of the Vernier effect-based sensor are given.

II. Principle and Mathematical Modeling

While the MWPI can be constructed based on different configurations, such as the Mach-Zehnder interferometer [28], [29] and the Michelson interferometer [30], [31], we have opted for a simple FPI structure in this work due to its compactness compared to the former two. The proposed self-Vernier effect is indeed generalizable and can be applied to other interferometric systems. A schematic diagram of the self-Vernier effect-based microwave-photonic FPI sensor system is shown in Fig. 1. The light signal from an amplified spontaneous emission (ASE) source after polarization controlling is intensity modulated by a radiofrequency signal from a vector network analyzer (VNA) via an electro-optic modulator (EOM). The intensity-modulated light is routed into an optical fiber circulator and used as the probing signal of the microwave-photonic FPI. The reflected signal from the FPI is sent into a highspeed photodetector (PD) for optoelectronic conversion, and the obtained electrical signal goes to the VNA for synchronized detection at the microwave modulation frequency. The microwave interferogram of the FPI is then obtained by linearly sweeping the modulation frequency and recording the magnitude and phase at each of the frequencies. Importantly, an additional optical path is introduced in the system, as shown in Fig. 1, with the assistance of two optical fiber couplers. The overlap between the signals transmitting through the two different paths with different optical delays generates the Vernier effect, i.e., the self-Vernier effect that magnifies the measurement sensitivity of the FPI. A variable optical delay line (VODL) can be included so that the delay of the additional path can be flexibly and easily adjusted, which determines the performance of the self-Vernier effect-based sensor, as it will be shown later.

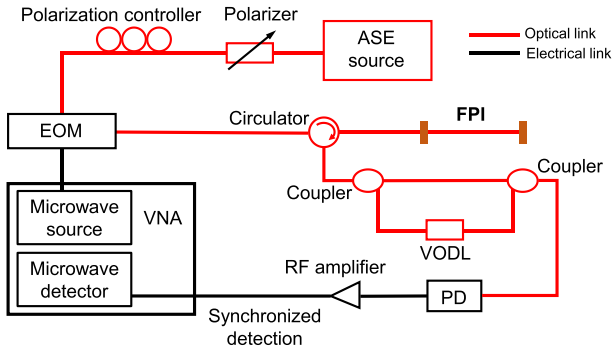

Fig. 1. The self-Vernier effect-based microwave-photonic FPI sensing system. An additional delay path with a variable optical delay line (VODL) is introduced with the assistance of two optical fiber couplers. ASE, amplified spontaneous emission; EOM, electro-optic modulator; VNA, vector network analyzer; PD, photodetector; RF amplifier, radiofrequency amplifier.

The FPI system shown in Fig. 1 operates in an incoherent regime where the OPD of the FPI is sufficiently larger than the coherence length of the broadband optical source (on the order of μm) [32]. Thus, the interference of the optical carrier signals can be neglected, and the interference of the reflected microwave envelope signals dominates. The complex frequency response after synchronized detection and normalization, i.e., S_{21}, can be expressed as [32]

$$S_{21} = \Gamma_1^2 T_1^2 e^{-j\Omega\frac{nZ_1}{c}} + \Gamma_1^2 T_2^2 e^{-j\Omega\left(\frac{nZ_1}{c}+\tau\right)} + \Gamma_2^2 T_1^2 e^{-j\Omega\left(\frac{nZ_1}{c}+t_0\right)} + \Gamma_2^2 T_2^2 e^{-j\Omega\left(\frac{nZ_1}{c}+t_0+\tau\right)}, \quad (1)$$

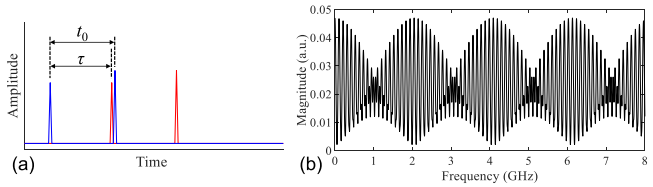

Fig. 2. Illustration of the self-Vernier effect as τ is close to t_0. (a) Time-domain illustration. The two red peaks represent the signals of the FPI after passing through the additional delay line. (b) Exemplary magnitude spectrum of the superimposed signal. The parameters used in the calculation are: $\Gamma_1 = 0.1$; $\Gamma_2 = 0.14$; $T_1 = 0.7$; $T_2 = 0.8$; $n = n_0 = 1.468$; $L_0 = 1$ m.

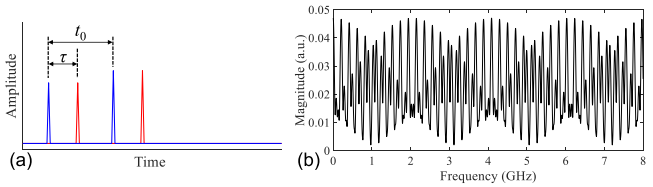

Fig. 3. Illustration of the self-Vernier effect as τ is close to $t_0/2$. (a) Time-domain illustration. The two red peaks represent the signals of the FPI after passing through the additional delay line. (b) Exemplary magnitude spectrum of the superimposed signal. The parameters used in the calculation are: $\Gamma_1 = 0.1$; $\Gamma_2 = 0.14$; $T_1 = 0.7$; $T_2 = 0.8$; $n = n_0 = 1.468$; $L_0 = 1$ m; $t_0/2 - \tau = 0.24$ ns, corresponding to an optical length of 0.0734 m.

where Γ_1 and Γ_2 are the reflection coefficient of the first reflector and second reflector of the FPI, respectively; Ω is the angular frequency of the microwave modulation signal; c is the speed of light in vacuum; T_1 and T_2 are the transmission coefficient of the original path and the additional path, respectively; n and Z_1 are the refractive index and total length of the common optical/electrical length in the system; τ is the optical delay introduced by the additional path, compared to the original path; and, t_0 is the time delay of the FPI and is given by

$$t_0 = \frac{OPD}{c} = \frac{2n_0 L_0}{c}, \tag{2}$$

where n_0 and L_0 are the refractive index and physical length of the FPI, respectively. According to (1), the magnitude spectrum of the complex S_{21} can be expressed as, (3) shown at the bottom of this page.

Thus, the magnitude spectrum is essentially the superposition of four different cosine signals with detuned frequencies, i.e., signals of four interferometers with detuned interference frequencies. The multiple frequencies give us the opportunity to flexibly choose two signals to generate the Vernier effect at the output spectrum, where only one interferometer is essentially involved, as expanded upon below.

A. Case I

Intuitively, when the introduced additional delay τ is set close to the delay of the FPI (t_0), i.e.,

$$\tau \approx t_0, \tag{4}$$

two cosine signals with slightly deviated frequencies are sustained in the output spectrum according to (3), i.e., $\cos(\Omega\tau)$ and $\cos(\Omega t_0)$, thereby generating the Vernier effect. Fig. 2(a) gives a schematic of the time-domain signal illustrating the case, which can be obtained by applying an inverse Fourier transform to the complex frequency response shown in (1). The amplitudes of the two reflected signals from the FPI are set different for the sake of clarity. Fig. 2(b) gives an example of the magnitude spectrum of the superimposed signal calculated based on (3), where the difference between τ and t_0 is set to ~0.49 ns, corresponding to an optical length of 0.1468 m. The free spectral range (FSR) of the envelope signal attributed to the overlap of the terms $\cos(\Omega\tau)$ and $\cos(\Omega t_0)$ is predicted by

$$FSR = \frac{(1/\tau)\cdot(1/t_0)}{|(1/\tau) - (1/t_0)|}. \tag{5}$$

The upper and lower envelopes shown in Fig. 2(b) are the desired signals that can be tracked for sensitivity-enhanced sensing with a magnification factor of

$$M \approx \frac{t_0}{t_0 - \tau}. \tag{6}$$

Thus, a smaller difference between the delay of the FPI (t_0) and the additional delay (τ) leads to a larger magnification factor, similar to conventional Vernier effect-based sensors [3]. Internal envelopes are also observed in the superimposed signal, which are induced by the so-called harmonic Vernier effect [33].

B. Case II

Interestingly, when the additional delay is half of the delay of the FPI, as schematically shown in Fig. 3(a), i.e.,

$$\tau \approx \frac{t_0}{2}, \tag{7}$$

the optical path length of the term $\cos(\Omega t_0)$ is approximately two times the optical length of the term $\cos(\Omega\tau)$, thus generating the so-called first-order microwave-photonic harmonic Vernier effect, as shown in Fig. 3(b), similar to the optical harmonic Vernier effect [33]. The FSR of the first-order harmonic envelope is predicted by

$$FSR = \frac{(1/\tau)\cdot(1/t_0)}{|(1/\tau) - 2\,(1/t_0)|}, \tag{8}$$

$$|S_{21}| = \sqrt{\begin{array}{l}\Gamma_1^4 T_1^4 + \Gamma_1^4 T_2^4 + \Gamma_2^4 T_1^4 + \Gamma_2^4 T_2^4 \\ +2\left(\Gamma_1^4 + \Gamma_2^4\right) T_1^2 T_2^2 \cos(\Omega\tau) + 2\Gamma_1^2\Gamma_2^2\left(T_1^4 + T_2^4\right)\cos(\Omega t_0) \\ +2\Gamma_1^2\Gamma_2^2 T_1^2 T_2^2 \cos\left[\Omega\left(\tau + t_0\right)\right] + 2\Gamma_1^2\Gamma_2^2 T_1^2 T_2^2 \cos\left[\Omega\left(\tau - t_0\right)\right]\end{array}}, \tag{3}$$

corresponding to the upper and lower envelopes. The sensitivity magnification factor can be expressed as

$$M \approx \frac{t_0}{t_0 - 2\tau}. \tag{9}$$

As investigated above, both cases can generate the self-Vernier effect that can be used to enhance the measurement sensitivity of the FPI.

It is worth mentioning that the variation of the additional delay path directly affects the performance of the self-Vernier effect-based sensor system. This, on one hand, provides the system with great flexibility for tuning the sensitivity magnification factor, but on the other hand, makes the system potentially more susceptible to environmental noises. To mitigate the detrimental effect, the additional delay path should be isolated from the environment, e.g., in a temperature-controlled box, as is the case for the 3-dB coupler-assisted Vernier effect sensor [34].

III. Experimental Results

A. Setup

The key components used to construct the microwave photonic FPI sensing system are listed as follows. ASE, C-band broadband light source (1528∼1563 nm); EOM, iXblue MXAN-LN-10; VNA, R&SZNB8; PD, KG-PD-20G. The length of the FPI used in the experiment was approximately 1.6 m. Tensile strains were applied to the FPI by stretching the fiber section using two translation stages (OMTOOLS, HFA-XYZ), affording a step-size resolution of 10 μm. The first reflector of the FPI was fabricated using an air-gap method [31], whereas the second reflector was the flat-cleaved end facet of the optical fiber. We used different lengths of optical fiber to function as the VODL in the additional delay line. All the experiments were performed at room temperature of 20 $\pm$ 1 °C.

B. Results

Case I was first verified in the experimental demonstration. An additional optical fiber length of approximately 3.1 m was introduced in the system shown in Fig. 1, corresponding to an optical length of 4.55 m, which is close to the OPD of the FPI of 4.70 m given the refractive index of the fiber to be 1.468. Fig. 4(a) gives the measured time-domain signal of the system, where four distinct peaks can be observed. The two blue peaks represent the reflected signals from the two reflectors of the FPI, whereas the two red peaks correspond to the delayed ones. From the time-domain signal, the time delay of the FPI (t_0) is determined to be 15.575 ns, and the additional delay τ is found to be 15.357 ns. As shown in the inset of Fig. 4(a), the first red peak approached the second blue peak, indicating that the additional delay τ is close to the delay t_0 of the FPI. Thus, a sensitivity magnification factor of 71 can be expected from the self-Vernier effect, compared to a conventional microwave-photonic FPI (without sensitivity amplification). Fig. 4(b) shows the measured magnitude spectrum of the system, which is generally similar to the calculated one shown in Fig. 2(b). The FSR of the upper and lower envelopes was found to be 4.8 GHz, close to the predicted value of 4.6 GHz according to (5).

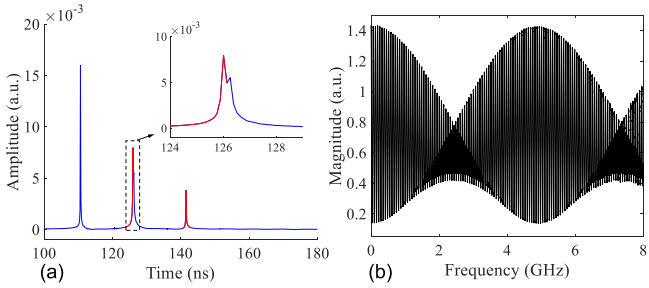

Fig. 4. Characterization of the FPI system with an additional time delay of ∼15.357 ns. (a) Measured time-domain signal of the system. The inset shows an enlarged view of the two adjacent peaks. (b) Measured magnitude spectrum in a frequency span of 8 GHz of the system.

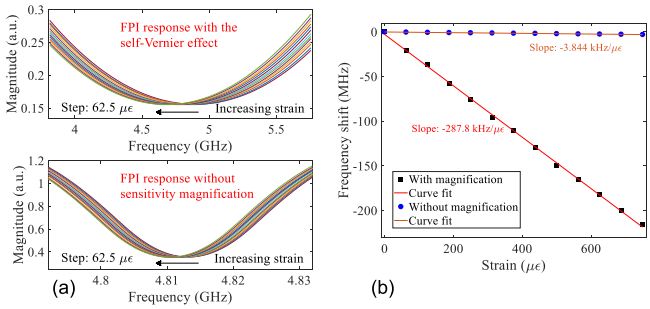

Fig. 5. Demonstration of the self-Vernier effect enhanced measurement sensitivity in case I. (a) Curve-fitted envelope signals for different settings of strains. The measured responses of the FPI without employing the self-Vernier effect are also shown for comparison. (b) Dip frequencies as a function of strain. The slopes (i.e., the measurement sensitivities) are obtained using linear curve fits.

Tensile strains were then applied to the FPI in the range of 750 $\mu\varepsilon$ with a step-size of 62.5$\mu\varepsilon$ to demonstrate the enhanced measurement sensitivity induced by the proposed self-Vernier effect. The magnitude spectrum of the system was measured and recorded at each strain step. The envelope of interest (i.e., the lower envelope) was then extracted by locating the series of minima in the spectrum, followed by a fourth-order polynomial curve fit to determine the dip frequency in the envelope signal. Note that the sampling points were set to as much as 20001 to minimize the errors introduced in determining the series of minima in the process of extracting the sensing envelope [35]. The output power from the ASE source was 30 mW to ensure that the reflected signal from the FPI can be effectively detected by the PD. Meanwhile, the signal-to-noise ratio (SNR) of the microwave modulation signals directly affects the SNR of the microwave interferogram. Thus, the intermediate frequency of the VNA was set to 1 kHz.

The dip frequency was then tracked in response to strains for sensitivity-enhanced sensing. Fig. 5(a) gives the curve-fitted envelope signals for different settings of applied strains, where an enlarged view of the measured magnitude spectra of the FPI without employing the self-Vernier effect for different settings of tensile strains is also shown for comparison. The spectrum shifted to the lower-frequency region in both cases, indicating

TABLE I
COMPARISON BETWEEN THE SELF-VERNIER SENSOR AND OTHER VERNIER STRAIN SENSORS

Sensing structures	Sensitivity (pm/με)	Dynamic range (με)	Magnification factor
Cascaded two FPIs [4]	47.14	200	29.5
Single FPI [36]	18.36	320	14.0
Separate two FPIs [11]	1150	160	N.A.
Cascaded two FPIs [20]	28.11	1500	23.8
Cascaded two FPIs [21]	145	200	N.A.
Separate two FPIs [34]	43.2	1750	4.6
Separate two FPIs [33]	93.4	600	27.7
Cascaded SI + modal interferometer [37]	65.71	300	20
Cascaded MZIs [38]	8.47	1000	5.4
Cascaded two rings [39]	911kHz/με	120	20
Single FPI [This work]	288 kHz/με	750	75 (Adjustable)

FPI, Fabry-Perot interferometer; SI, Sagnac interferometer; MZI, Mach-Zehnder interferometer; N.A., not available.

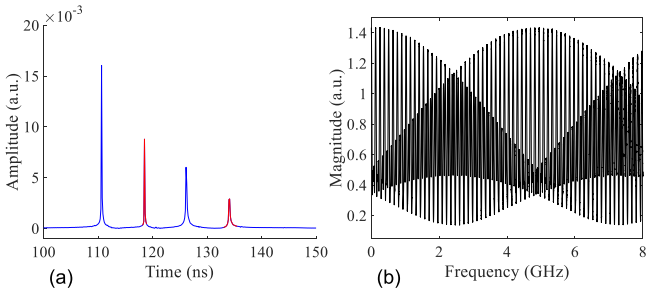

Fig. 6. Characterization of the system with an additional time delay of ∼7.886 ns. (a) Measured time-domain signal of the system. The two red peaks correspond to the FPI signal transmitting through the additional delay line. (b) Measured magnitude spectrum in a frequency span of 8 GHz of the system.

a positive magnification factor. The dip frequencies were determined from Fig. 5(a), and linear curve fits were employed to find out the measurement sensitivities, as shown in Fig. 5(b). The self-Vernier effect-based FPI sensor showed a sensitivity of -287.8 kHz/$\mu\varepsilon$ with a linear coefficient of 0.9993, whereas the FPI without magnification showed a sensitivity of only -3.844 kHz/$\mu\varepsilon$, revealing a sensitivity magnification factor of 75, which matches well with the theoretically predicted factor of 71. A comparison between the proposed self-Vernier strain sensor with the state-of-the-art Vernier strain sensors is given in Table I. It is shown that the proposed self-Vernier sensor can achieve simultaneously a large dynamic range and high sensitivity magnification based on a single FPI configuration.

Next, the optical fiber length of the additional fiber delay line was decreased to verify Case II, where the additional delay τ was reduced to 7.886 ns, which approaches half of the time delay of the FPI ($t_0 = 15.575$ ns). Fig. 6(a) shows the measured time-domain signal of the modified system, where four peaks with approximately equal intervals were observed, as expected. The measured magnitude spectrum of the system is given in Fig. 6(b).

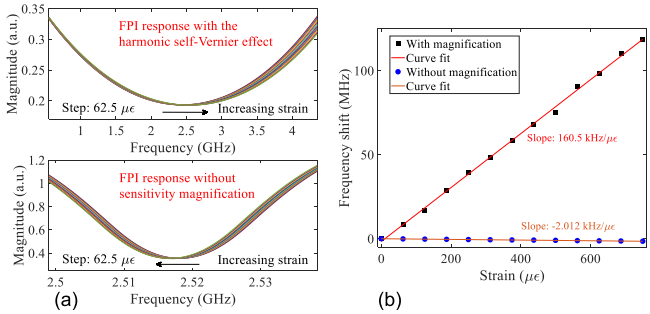

Fig. 7. Demonstration of the harmonic self-Vernier effect enhanced measurement sensitivity in case II. (a) Curve-fitted envelope signals for different settings of strains. The measured responses of the FPI without employing the harmonic self-Vernier effect are also included. (b) Dip frequencies as a function of strains.

The FSR of the lower envelope signal was determined to be ∼4.9 GHz, matching the predicted value of 5 GHz according to (8).

The same strain experiments were performed, followed by the same signal processing procedures as discussed above. Fig. 7(a) plots the curve-fitted envelope signals (the lower envelope) for different settings of tensile strains applied to the FPI sensor, where the interference signals of the FPI without employing the self-Vernier effect centered at ∼2.5 GHz are also shown. Different from the results shown in Fig. 5(a), the envelope signal shifted to the higher-frequency region as the applied strain increased, from which a negative magnification factor can be inferred. The dip frequencies as a function of applied strains are shown in Fig. 7(b). Linear curve fits were applied to find the slopes of the two measurements, revealing measurement sensitivities of 160.5 kHz/$\mu\varepsilon$ and -2.012 kHz/$\mu\varepsilon$. The results indicate a sensitivity magnification factor of 80 with a negative sign, which agrees with the theoretical factor of 79, as can be expected from (9).

It is important to note that in addition to strain, the sensitivity of the sensor to temperature variations and other variables (e.g., vibrations) was also magnified by the self-Vernier effect, which could contribute to increased errors during strain measurements. In fact, as can be observed in Figs. 5(b) and 7(b), the measurement uncertainty was also magnified. The increased deviation from the linear curve fit model is attributed to the additional errors introduced in extracting the sensing envelope, the magnified temperature cross-sensitivity induced errors, as well as the magnified system noise due to the self-Vernier effect [35]. Nevertheless, the experimental results shown in Figs. 4–7 demonstrate the feasibility of the proposed self-Vernier effect and the associated harmonic self-Vernier effect for sensitivity amplification of a microwave-photonic FPI sensor. The sensitivity magnification factor can be flexibly tuned by adjusting the additional time delay introduced in the system. The self-Vernier effect is also generalizable and can be extended to other microwave-photonic interferometers and resonators for sensitivity amplification.

IV. MACHINE LEARNING ANALYSIS

As noted in a recent critical review [3], one of the largest downsides of Vernier effect-based optical fiber sensors is the interrogation system, which typically involves an ultra-broadband light source and a bulky optical spectrum analyzer. The optical

spectrum of the Vernier effect-based sensor must be acquired over a large range of wavelengths, followed by cumbersome signal processing, from which the Vernier envelope is extracted and then used as the sensing signal. In the case of microwave-photonic Vernier effect-based sensors (including the proposed self-Vernier effect-based), a VNA is used, and the microwave spectrum of the sensor is measured over a broad range of frequencies (several GHz). Similar and yet complex signal processing procedures involving multiple nonlinear approximations are employed to obtain the envelope signal, as discussed in Section III. Intrigued by the success of machine learning techniques in various fields, from conventional machine vision [40], [41] to biology [42], [43], as well as ultrafast photonics [44], [45], communication [46], and sensing [47], [48], [49], we present the first attempt to employ machine learning as a tool for the demodulation of Vernier effect-based sensors.

A. Gaussian Process Regression-Based Demodulation

While there are various supervised machine learning models (e.g., neural networks, support vector machine), we opted for Gaussian process regression (GPR) in this work because GPR generally works well on small datasets and provides empirical confidence intervals on the predictions [50], [51], [52]. These two aspects are of significant importance in the field of sensing, as the former can simplify the sensor calibration process while the latter can provide uncertainty measures of the sensor.

Different from conventional curve fit methods where a specific fitting model must be designated, GPR is a nonparametric Bayesian approach to regression. One of the most important parameters of a GPR model is the kernel, which describes a measure of similarity between the input data sets. The kernel chosen in this work is the rational quadratic covariance function given by

$$k\left(x_i, x_j\right) = \left(1 + \frac{d(x_i, x_j)^2}{2\alpha l^2}\right)^{-\alpha}, \tag{10}$$

where x_i and x_j are the two input datasets; d is the Euclidean distance; and, α and l are the scale mixture parameter and the length scale of the kernel, respectively. In the case of using GPR for the demodulation of the self-Vernier effect-based sensor, a training dataset, including inputs and corresponding targets, needs to be acquired first. The inputs would simply be the measured spectra of the sensor, and the corresponding settings of tensile strains are considered the targets. The hyperparameters of the GPR kernel are then optimized using the training dataset by making a series of predictions. Specifically, four covariance matrices are calculated in a prediction, which reveals the relation that the data points have with each other in the training data predicated by the kernel, and can be given by [51]

$$\begin{aligned} \mathrm{K} &= k\left(\mathrm{X}_{1:N}, \mathrm{X}_{1:N}\right) \\ \mathrm{K}_* &= k\left(\mathrm{X}_{1:N}, \mathrm{X}_*\right) \\ \mathrm{K}_*^{\mathrm{T}} &= k\left(\mathrm{X}_*, \mathrm{X}_{1:N}\right) \\ \mathrm{K}_{**} &= k\left(\mathrm{X}_*, \mathrm{X}_*\right), \end{aligned} \tag{11}$$

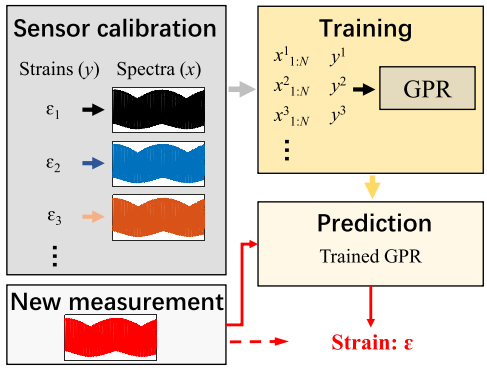

Fig. 8. Overview of the GPR-based demodulation approach for the Vernier effect-based sensor. Each of the spectra for a specific setting of strain consists of N sampling points.

where $\mathrm{X}_{1:N}$ and X_* are the training input data and target data, respectively. By calculating the covariance matrices, a prediction can be made [51]

$$\begin{aligned} y_* &= \mathrm{K}_*^{\mathrm{T}}\left(\mathrm{K} + \sigma^2\mathrm{I}\right)^{-1} y \\ \mathrm{Var}(y_*) &= \mathrm{K}_{**} - \mathrm{K}_*^{\mathrm{T}}\left(\mathrm{K} + \sigma^2\mathrm{I}\right)^{-1}\mathrm{K}_* \end{aligned}, \tag{12}$$

where y_* and y are the predicted target and training target (i.e., strains); Var denotes the uncertainty of the prediction of y_*; σ is a hyperparameter; and, I is the identity matrix. The abovementioned prediction is utilized to optimize the associated hyperparameters (i.e., α, l, and σ) by minimizing the error between the predicted target and the training target. Five-fold cross-validation is employed to avoid overfitting. The root mean square error (RMSE) is considered the quality measure of the trained model. Once the hyperparameters are optimized, an unknown strain can be accurately predicted by the GPR model by directly feeding the measured raw spectrum into the model. An overview of the demodulation process using GPR for the Vernier sensor is shown in Fig. 8.

B. Training and Prediction Results

Tensile strains ranging from 0 to 1000 $\mu\varepsilon$ in steps of 62.5 $\mu\varepsilon$ were applied to a microwave-photonic FPI system operating in Case II based on the self-Vernier effect. A theoretical sensitivity magnification factor of ~63 could be expected from the sensor. At each strain step, ten measurements of the microwave spectrum were performed using the VNA, similar to the standard optical sensor calibration process. The VNA was configured with total sampling points of 20001, a frequency span of 8 GHz, and an intermediate frequency bandwidth of 1 kHz. The GPR model training was performed in Matlab on a laptop with 16.0 GB RAM and an i7 2.30 GHz CPU.

In the sensor calibration process, a total of 170 spectra (each including 20001 sampling points) were obtained. The spectra at the strain setting of 62.5 $\mu\varepsilon \times i$ (where i is an even number, i.e., 0, 2, 4, …, 16) were used to train the GPR model, where the corresponding strains were used as the targets, resulting in a 20002-by-90 matrix as the training dataset. The rest 80 spectra (at the strain setting of 62.5 $\mu\varepsilon \times i$, i = 1, 3, 5, …, 15) were

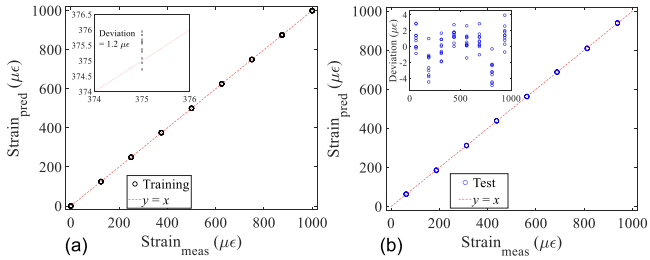

Fig. 9. GPR-based demodulation. (a) Scatter plot of training data obtained from the GPR model, comparing the predicted strains and measured strains (ground truth) along the ideal model (the red dashed line, $y = x$). Inset shows the largest deviation obtained for the training data. (b) Comparing the predicted and measured values using the trained GPR model for a series of unknown strains (test data). The inset gives the prediction errors for the test data.

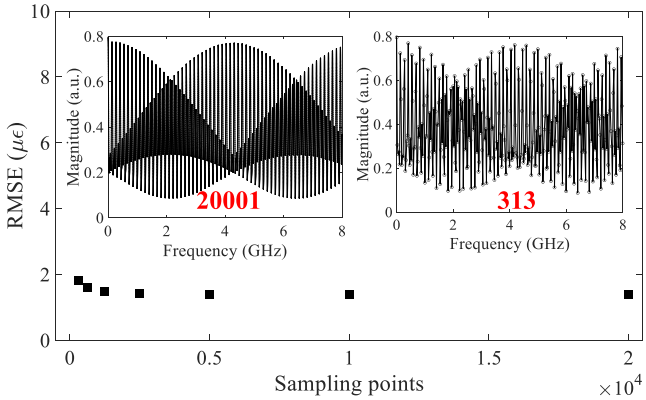

Fig. 10. RMSE of the trained GPR models with respect to sampling points of the measured spectra of the sensor. The inset figures give the exemplary spectra of the sensor with different sampling points (i.e., 20001 and 313).

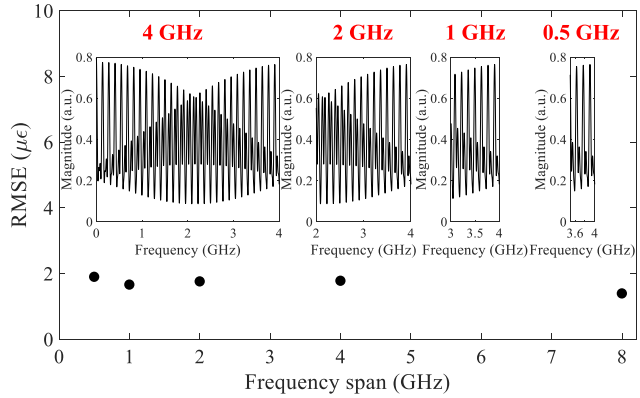

Fig. 11. RMSE of the trained GPR models with respect to measurement frequency spans of the sensor spectra. The insets give the exemplary spectra of the sensor with different sampling spans.

used as the unseen data to test the performance of the trained GPR model. The predicted strains obtained from the GPR model during the training process are plotted against the actual strains applied in the experiment in Fig. 9(a); the closer these dots to the $y = x$ (as indicated by the red dashed line), the better the trained model. The inset in Fig. 9(a) gives an enlarged view of the predicted strains at a setting of 375 $\mu\varepsilon$, showing the largest deviation of 1.2 $\mu\varepsilon$. Next, we have compared the predicted strains and the corresponding actual values employing the trained GPR model for a series of unknown strains (test data), as shown in Fig. 9(b). Slightly Increased prediction errors of $\sim$4 $\mu\varepsilon$ can be observed in the inset of Fig. 9(b). We think this is reasonable given the fact that only a small dataset was utilized in the training process. An overall RMSE of 1.4 $\mu\varepsilon$ was obtained for the GPR prediction, which is beyond the limit of detection of conventional incoherent microwave-photonic interferometers. Thus, GPR can be used as a simple, efficient, and effective tool for the demodulation of Vernier effect-based sensors, where the measurement parameter is directly mapped to the raw spectrum of the sensor, avoiding cumbersome and complex data processing as encountered in traditional approaches.

Additional calculations were performed to further investigate the potential of GRP for the demodulation of the Vernier sensor. In the case of the conventional demodulation method, the spectrum of a Vernier sensor must be acquired in a broad wavelength (frequency) range with sufficient sampling points, representing a penalty on the system cost as well as the data acquisition time. Here, we show that by using GPR for the demodulation, both the frequency span and the sampling points for the Vernier sensor can be remarkably reduced and yet without sacrificing the measurement accuracy of the sensor, which would have been impossible for the conventional approach. Details are given as follows.

The same data set (a total of 170 spectra) and training/test processes were used in the following investigation. The difference is that each of the spectra was first down-sampled and then used as the input for training and testing a new GPR model. Fig. 10 gives the obtained RMSE of the GPR models when fed with spectra with different sampling points. A slight increase in the RMSE from 1.4 $\mu\varepsilon$ to 1.8 $\mu\varepsilon$ was observed as the sampling points decreased from 5001 to 313, which demonstrates the capability of the GPR approach given the fact that the spectrum with only 313 points is severely distorted as shown in the inset of Fig. 10.

We also resampled each of the spectra at different frequency spans and used the resampled spectra to train and test new GPR models. The insets in Fig. 11 give a few spectra of the sensor sampled with frequency spans of 4, 2, 1, and 0.5 GHz. Note that when the sampling frequency span is reduced to 2 GHz (smaller than the FSR of the envelope signal), the dip frequency of the envelope signal might not be included in the spectrum, making it challenging to analyze the spectral shift using the conventional dip tracking method. Thus, machine learning (e.g., GPR) can be used to address this issue. Fig. 11 plots the RMSE of GPR models with respect to the frequency spans of the spectra utilized to train the models. No significant increases in RSME were observed as the frequency span decreased down to 0.5 GHz, where only a few interference fringe dips were included in the spectrum. The results shown in Figs. 10 and 11 verify that the stringent requirement of the measured spectrum from the Vernier sensor, including the frequency span and sampling points, can be significantly alleviated by using GPR as a demodulation tool, which would ultimately lead to a huge decrease in the complexity

and cost of the interrogation system of Vernier effect-based sensors.

V. Conclusion

We have proposed and demonstrated a new concept of the self-Vernier effect using an incoherent microwave-photonic interferometer, where the Vernier effect is generated by overlapping the interference spectra of an interferometer and its time-delayed one. Two different situations have been theoretically and experimentally investigated, covering the fundamental Vernier effect and the harmonic Vernier effect, and both have shown flexible and efficient sensitivity magnification. We have also proposed the use of machine learning (e.g., GPR) to directly learn the relationship between the measurement parameter (i.e., tensile strain) and the raw spectrum acquired from the Vernier sensor, without any complex and cumbersome nonlinear curve fitting processes. We have also shown that the sampling points and measurement frequency bandwidth of the spectra of the Vernier sensor can be greatly reduced by employing GPR-based analysis.

The present work is dedicated to accelerating the development of the Vernier effect-based sensors. The proposed self-Vernier effect helps to simplify the hardware design of the Vernier sensor system, where the Vernier effect can be obtained using only a single interferometer. The use of machine learning to demodulate the sensor represents an advancement from the software aspect and gives an entirely new route to the signal processing of Vernier sensors. We envision that further optimization of the proposed two techniques could ultimately lead to a new generation of simpler, cheaper, and faster interrogation systems for Vernier effect-based sensors, facilitating the acceptance and utilization of the Vernier effect as a practical and efficient approach to sensitivity magnification of optical fiber sensors.

References

[1] R. Xu, S. Liu, Q. Sun, P. Lu, and D. Liu, "Experimental characterization of a Vernier strain sensor using cascaded fiber rings," *IEEE Photon. Technol. Lett.*, vol. 24, no. 23, pp. 2125–2128, Dec. 2012.

[2] Y. Liu, X. Li, Y.-N. Zhang, and Y. Zhao, "Fiber-optic sensors based on Vernier effect," *Measurement*, vol. 167, 2021, Art. no. 108451.

[3] A. D. Gomes, H. Bartelt, and O. Frazão, "Optical Vernier effect: Recent advances and developments," *Laser Photon. Rev.*, vol. 15, no. 7, 2021, Art. no. 2000588.

[4] P. Zhang et al., "Cascaded fiber-optic Fabry-Perot interferometers with Vernier effect for highly sensitive measurement of axial strain and magnetic field," *Opt. Exp.*, vol. 22, no. 16, pp. 19581–19588, 2014.

[5] Y. Chen, L. Zhao, S. Hao, and J. Tang, "Advanced fiber sensors based on the Vernier effect," *Sensors*, vol. 22, no. 7, 2022, Art. no. 2694.

[6] M. L. Notte, B. Troia, T. Muciaccia, C. E. Campanella, F. De Leonardis, and V. M. Passaro, "Recent advances in gas and chemical detection by Vernier effect-based photonic sensors," *Sensors*, vol. 14, no. 3, pp. 4831–4855, 2014.

[7] Y. Zhao et al., "Ultrasensitive temperature sensor with Vernier-effect improved fiber Michelson interferometer," *Opt. Exp.*, vol. 29, no. 2, pp. 1090–1101, 2021.

[8] P. Zhang et al., "Simplified hollow-core fiber-based Fabry–Perot interferometer with modified Vernier effect for highly sensitive high-temperature measurement," *IEEE Photon. J.*, vol. 7, no. 1, Feb. 2015, Art. no. 7100210.

[9] A. D. Gomes et al., "Multimode Fabry–Perot interferometer probe based on Vernier effect for enhanced temperature sensing," *Sensors*, vol. 19, no. 3, 2019, Art. no. 453.

[10] P. M. R. Robalinho, A. D. Gomes, and O. Frazao, "High enhancement strain sensor based on Vernier effect using 2-fiber loop mirrors," *IEEE Photon. Technol. Lett.*, vol. 32, no. 18, pp. 1139–1142, Sep. 2020.

[11] J. Tian, Z. Li, Y. Sun, and Y. Yao, "High-sensitivity fiber-optic strain sensor based on the Vernier effect and separated Fabry–Perot interferometers," *J. Lightw. Technol.*, vol. 37, no. 21, pp. 5609–5618, 2019.

[12] L. G. Abbas, "Vernier effect-based strain sensor with cascaded Fabry–Pérot interferometers," *IEEE Sens. J.*, vol. 20, no. 16, pp. 9196–9201, Aug. 2020.

[13] Y. Yang, X. Zhang, L. Yang, Y. Yu, Z. Wang, and T. Wang, "Ultrahigh-sensitivity displacement sensing enabled by the Vernier effect with inhibited antiresonance," *Opt. Lett.*, vol. 46, no. 5, pp. 1053–1056, 2021.

[14] C. Zhou, Q. Zhou, B. Wang, J. Tian, and Y. Yao, "High-sensitivity relative humidity fiber-optic sensor based on an internal–external Fabry–Perot cavity Vernier effect," *Opt. Exp.*, vol. 29, no. 8, pp. 11854–11868, 2021.

[15] C. Zhou, Y. Song, Q. Zhou, J. Tian, and Y. Yao, "Ultra-high-sensitivity humidity fiber sensor based on harmonic Vernier effect in cascaded FPI," *Sensors*, vol. 22, no. 13, 2022, Art. no. 4816.

[16] M. Quan, J. Tian, and Y. Yao, "Ultra-high sensitivity Fabry–Perot interferometer gas refractive index fiber sensor based on photonic crystal fiber and Vernier effect," *Opt. Lett.*, vol. 40, no. 21, pp. 4891–4894, 2015.

[17] J. Li et al., "Ultrasensitive refractive index sensor based on enhanced Vernier effect through cascaded fiber core-offset pairs," *Opt. Exp.*, vol. 28, no. 3, pp. 4145–4155, 2020.

[18] Z. Xu et al., "Highly sensitive refractive index sensor based on cascaded microfiber knots with Vernier effect," *Opt. Exp.*, vol. 23, no. 5, pp. 6662–6672, 2015.

[19] Z. Xu, Y. Luo, D. Liu, P. P. Shum, and Q. Sun, "Sensitivity-controllable refractive index sensor based on reflective θ-shaped microfiber resonator cooperated with Vernier effect," *Sci. Rep.*, vol. 7, no. 1, pp. 1–8, 2017.

[20] J. Deng and D. Wang, "Ultra-sensitive strain sensor based on femtosecond laser inscribed in-fiber reflection mirrors and Vernier effect," *J. Lightw. Technol.*, vol. 37, no. 19, pp. 4935–4939, 2019.

[21] T. Paixão, F. Araújo, and P. Antunes, "Highly sensitive fiber optic temperature and strain sensor based on an intrinsic Fabry–Perot interferometer fabricated by a femtosecond laser," *Opt. Lett.*, vol. 44, no. 19, pp. 4833–4836, 2019.

[22] A. D. Gomes et al., "Giant refractometric sensitivity by combining extreme optical Vernier effect and modal interference," *Sci. Rep.*, vol. 10, no. 1, pp. 1–14, 2020.

[23] X. Fang et al., "Signal processing assisted Vernier effect in a single interferometer for sensitivity magnification," *Opt. Exp.*, vol. 29, no. 8, pp. 11570–11581, 2021.

[24] C. Zhu and J. Huang, "Sensitivity-enhanced microwave-photonic optical fiber interferometry based on the Vernier effect," *Opt. Exp.*, vol. 29, no. 11, pp. 16820–16832, 2021.

[25] Z. Xu, X. Shu, and H. Fu, "Sensitivity enhanced fiber sensor based on a fiber ring microwave photonic filter with the Vernier effect," *Opt. Exp.*, vol. 25, no. 18, pp. 21559–21566, 2017.

[26] Z. Xu and X. Shu, "Fiber optic sensor based on Vernier microwave frequency comb," *J. Lightw. Technol.*, vol. 37, no. 14, pp. 3503–3509, 2019.

[27] C. Zhu, M. Roman, Y. Zhuang, and J. Huang, "Distributed fiber optic sensing with enhanced sensitivity based on microwave-photonic Vernier effect," *Opt. Lett.*, vol. 47, no. 11, pp. 2810–2813, 2022.

[28] T. Wei, J. Huang, X. Lan, Q. Han, and H. Xiao, "Optical fiber sensor based on a radio frequency Mach–Zehnder interferometer," *Opt. Lett.*, vol. 37, no. 4, pp. 647–649, 2012.

[29] C. Zhu, R. E. Gerald, and J. Huang, "Ultra-sensitive microwave-photonic optical fiber interferometry based on phase-shift amplification," *IEEE J. Sel. Topics Quantum Electron.*, vol. 27, no. 6, Nov./Dec. 2021, Art. no. 5600408.

[30] M. Deng et al., "Enhanced sensitivity of optical fiber vibration sensor based on radio-frequency Michelson interferometer," *Opt. Lett.*, vol. 46, no. 24, pp. 6079–6082, 2021.

[31] C. Zhu and J. Huang, "Microwave-photonic optical fiber interferometers for refractive index sensing with high sensitivity and a tunable dynamic range," *Opt. Lett.*, vol. 46, no. 9, pp. 2180–2183, 2021.

[32] L. Hua, Y. Song, B. Cheng, W. Zhu, Q. Zhang, and H. Xiao, "Coherence-length-gated distributed optical fiber sensing based on microwave-photonic interferometry," *Opt. Exp.*, vol. 25, no. 25, pp. 31362–31376, 2017.

[33] A. D. Gomes et al., "Optical harmonic Vernier effect: A new tool for high performance interferometric fiber sensors," *Sensors*, vol. 19, no. 24, 2019, Art. no. 5431.

[34] T. Nan et al., "Ultrasensitive strain sensor based on Vernier-effect improved parallel structured fiber-optic Fabry-Perot interferometer," *Opt. Exp.*, vol. 27, no. 12, pp. 17239–17250, 2019.
[35] Y. Li, Y. Li, Y. Liu, Y. Li, and S. Qu, "Detection limit analysis of optical fiber sensors based on interferometers with the Vernier-effect," *Opt. Exp.*, vol. 30, no. 20, pp. 35734–35748, 2022.
[36] Y. Wu, L. Xia, W. Li, and J. Xia, "Highly sensitive Fabry–Perot demodulation based on coarse wavelength sampling and Vernier effect," *IEEE Photon. Technol. Lett.*, vol. 31, no. 6, pp. 487–490, Mar. 2019.
[37] L. Liu et al., "High-sensitivity strain sensor implemented by hybrid cascaded interferometers and the Vernier-effect," *Opt. Laser Technol.*, vol. 119, 2019, Art. no. 105591.
[38] M. Xie, H. Gong, J. Zhang, C.-L. Zhao, and X. Dong, "Vernier effect of two cascaded in-fiber Mach–Zehnder interferometers based on a spherical-shaped structure," *Appl. Opt.*, vol. 58, no. 23, pp. 6204–6210, 2019.
[39] Y. Zhang, B. Xu, D. Wang, H. Gong, Y. Li, and C.-L. Zhao, "Sensitivity-enhanced fiber strain sensing system based on microwave frequency scanning with the Vernier effect," *Opt. Fiber Technol.*, vol. 43, pp. 175–179, 2018.
[40] N. Sebe, I. Cohen, A. Garg, and T. S. Huang, *Machine Learning in Computer Vision*. Berlin, Germany: Springer, 2005.
[41] L. Zhu, P. Spachos, E. Pensini, and K. N. Plataniotis, "Deep learning and machine vision for food processing: A survey," *Curr. Res. Nutr. Food Sci.*, vol. 4, pp. 233–249, 2021.
[42] D. T. Jones, "Setting the standards for machine learning in biology," *Nature Rev. Mol. Cell Biol.*, vol. 20, no. 11, pp. 659–660, 2019.
[43] M. Zitnik, F. Nguyen, B. Wang, J. Leskovec, A. Goldenberg, and M. M. Hoffman, "Machine learning for integrating data in biology and medicine: Principles, practice, and opportunities," *Inf. Fusion*, vol. 50, pp. 71–91, 2019.
[44] G. Genty et al., "Machine learning and applications in ultrafast photonics," *Nature Photon.*, vol. 15, no. 2, pp. 91–101, 2021.
[45] D. Zibar, H. Wymeersch, and I. Lyubomirsky, "Machine learning under the spotlight," *Nature Photon.*, vol. 11, no. 12, pp. 749–751, 2017.
[46] O. Simeone, "A very brief introduction to machine learning with applications to communication systems," *IEEE Trans. Cogn. Commun. Netw.*, vol. 4, no. 4, pp. 648–664, Dec. 2018.
[47] A. Venketeswaran et al., "Recent advances in machine learning for fiber optic sensor applications," *Adv. Intell. Syst.*, vol. 4, no. 1, 2022, Art. no. 2100067.
[48] C. Zhu, R. E. Gerald, II, Y. Chen, and J. Huang, "One-dimensional sensor learns to sense three-dimensional space," *Opt. Exp.*, vol. 28, no. 13, pp. 19374–19389, 2020.
[49] L. V. Nguyen, C. C. Nguyen, G. Carneiro, H. Ebendorff-Heidepriem, and S. C. Warren-Smith, "Sensing in the presence of strong noise by deep learning of dynamic multimode fiber interference," *Photon. Res.*, vol. 9, no. 4, pp. B109–B118, 2021.
[50] C. K. Williams and C. E. Rasmussen, *Gaussian Processes for Machine Learning*. Cambridge, MA, USA: MIT Press, 2006.
[51] M. S. E. Djurhuus, S. Werzinger, B. Schmauss, A. T. Clausen, and D. Zibar, "Machine learning assisted fiber bragg grating-based temperature sensing," *IEEE Photon. Technol. Lett.*, vol. 31, no. 12, pp. 939–942, Jun. 2019.
[52] C. Luo, D. Zheng, X. Zou, W. Pan, and L. Yan, "Performance upgradation of microwave photonic filtering interrogation using Gaussian process regression," *J. Lightw. Technol.*, vol. 39, no. 24, pp. 7682–7688, 2021.

Chen Zhu (Member, IEEE) received the B.E. degree in optoelectronics information engineering from the Huazhong University of Science and Technology, Wuhan, China, in 2015, and the Ph.D. degree in electrical engineering from the Missouri University of Science and Technology, Rolla, MO, USA, in 2021. He is currently a Principal Investigator with the Zhejiang Laboratory, Research Center for Optical Fiber Sensing, Hangzhou, China. He was an Assistant Research Professor of electrical and computer engineering with the Missouri University of Science and Technology. He has authored or coauthored more than 50 refereed articles, ten conference papers, and one book chapter. His research focuses on the development of fiber optic and microwave devices for sensing applications in harsh environments. Dr. Zhu was the recipient of the IEEE Instrumentation and Measurement Society Graduate Fellowship Award from 2018 to 2019 and 2020 IEEE St. Louis Section Outstanding Graduate Student Award.

Jie Huang (Senior Member, IEEE) received the Ph.D. degree in electrical engineering from Clemson University, Clemson, Clemson, SC, USA, in 2015. He is currently the Roy A. Wilkens Endowed Associate Professor of electrical and computer engineering with the Missouri University of Science and Technology, Rolla, MO, USA. He established the Lightwave Technology Laboratory with a strong track record of sustained research funding, high-quality journal publications, and state-of-the-art research infrastructure with cutting-edge capabilities. He has authored or coauthored more than 100 refereed articles, 70 conference papers, one book chapter, and ten U.S. patent applications, in the arena of advanced sensors. His research interests include the development of optical and microwave sensors and instrumentation for applications in energy, intelligent infrastructures, clean environments, biomedical sensing, and harsh environments.